EFDA–JET–PR(14)10

T. Rafiq, A.H. Kritz, V. Tangri, A.Y. Pankin,
I. Voitsekhovitch, R.V. Budny and JET EFDA contributors

Comparison of Simulation and Experimental Temperature Profiles in L-Mode Tokamak Plasmas Using an Improved Multi-Mode Model

Comparison of Simulation and Experimental Temperature Profiles in L-Mode Tokamak Plasmas Using an Improved Multi-Mode Model

T. Rafiq[1], A.H. Kritz[1], V. Tangri[1], A.Y. Pankin[2],
I. Voitsekhovitch[3], R.V. Budny[4] and JET EFDA contributors*

JET-EFDA, Culham Science Centre, OX14 3DB, Abingdon, UK

[1]*Department of Physics, Lehigh University, Bethlehem, PA, US*
[2]*Tech-X Corporation, Boulder, CO, US*
[3]*CCFE, Culham Science Centre, Abingdon, Oxon, OX14 3DB, UK*
[4]*Princeton Plasma Physics Laboratory, Princeton, NJ, US*
** See annex of F. Romanelli et al, "Overview of JET Results", (24th IAEA Fusion Energy Conference, San Diego, USA (2012)).*

Preprint of Paper to be submitted for publication in
Physics of Plasmas

ABSTRACT

Simulations of DIII-D, JET and TFTR L-mode tokamak plasmas are carried out using the PTRANSP predictive integrated modeling code. The simulation and experimental temperature profiles are compared. The time evolved temperature profiles are computed utilizing the Multi-Mode anomalous transport model version 7.1 (MMM7.1) which includes transport associated with drift-resistive-inertial ballooning modes (the DRIBM model [T. Rafiq, et. al, Physics of Plasmas **17**, 082511 (2010)]). The tokamak discharges considered involved a broad range of conditions including scans over gyroradius, ITER like current ramp-up, with and without neon impurity injection, collisionality, and low and high plasma current. The comparison of simulation and experimental temperature profiles for the discharges considered is shown for the radial range from the magnetic axis to the last closed flux surface. The regions where various modes in the Multi-Mode model contribute to transport are illustrated. In the simulations carried out using the MMM7.1 model it is found that: The drift-resistive-inertial ballooning modes contribute to the anomalous transport primarily near the edge of the plasma; transport associated with the ion temperature gradient and trapped electron modes contribute in the core region but decrease in the region of the plasma boundary; and neoclassical ion thermal transport contributes mainly near the center of the discharge.

I. INTRODUCTION

Predictive simulations are carried out utilizing the Multi-Mode anomalous transport model version 7.1 (MMM7.1) in order to illustrate that the predictions of electron and ion thermal transport yield temperature profiles that are consistent with profiles measured in L-mode discharges in the Doublet III-D (DIII-D), the Joint European Tokamak (JET) and the Tokamak Fusion Test Reactor (TFTR).

The Lehigh Fusion Physics Group has focused for a number of years on the development of models for anomalous transport for tokamak plasmas. Members of the Lehigh group have developed a new Multi Mode anomalous transport model MMM7.1 [1] to replace the older MMM95 transport model [2] that was used for more than a decade. The predictions provided by the MMM95 model have been verified against other anomalous transport models such

as GLF23 and validated using experimental data from the Alcator C-Mod, DIII-D, TFTR, JET and Tore-Supra tokamaks [3–7]. The MMM95 model was used together with models for neoclassical transport and sources of heating and current drive in integrated modeling codes in order to compute the evolution of temperature, density and magnetic-q profiles in tokamak plasma discharges.

The MMM7.1 computation of transport for plasma regions with low and reverse magnetic shear and finite plasma β (ratio of plasma to magnetic pressure) is based on an improved theoretical foundation. The MMM7.1 model includes a theory-based prediction of momentum transport, which was not available in the MMM95 model, and also includes a model for transport driven by electron temperature gradient modes. The earlier MMM95 model contained an empirical based resistive ballooning mode model. This empirical model is replaced with a theory based drift resistive inertial ballooning mode (DRIBM) model [8]. Inclusion of the contributions to transport, resulting from drift resistive inertial ballooning modes, are necessary for simulations that include the low temperature edge region of L-mode and Ohmic tokamak discharges.

The development of the Multi-Mode model has been guided by the philosophy of using in integrated whole device simulations a combination of models, that are based on the best available theoretically derived models, in order to produce predictive integrated modeling results that are consistent with experimental data. In this research plasma profiles, obtained in simulations using the Multi-Mode model, are compared with experimental profiles in order to examine the aspects and components of the model that provide agreement with data under a wide range of conditions for a number of tokamaks as well as to determine the aspects and components of the Multi-Mode model that require improvement. Not only the strengths and weaknesses of each component model is acquired, but it is also learned how a component model works together with other models in the comprehensive integrated simulations.

The MMM7.1 model [1] that has been developed and tested includes transport driven by instabilities associated with the ion temperature gradient (ITG), trapped electron (TE), kinetic ballooning (KB), collisionless and collision dominated magnetohydrodynamic modes (Weiland model by J. Weiland and his group at Chalmers University in Sweden [9]), DRIBM modes (Rafiq model for Drift-resistive-inertial ballooning modes [8]) and ETG modes (Horton model for anomalous transport driven by Electron Temperature Gradient (ETG) modes [10] with the Jenko threshold [11]). The combination of modes in MMM7.1

is required in order to include the transport associated with ion and electron temperature and density gradients, resistive effects, and electron trapping.

The MMM7.1 transport model is documented and organized as a stand-alone model, which fully complies with the National Transport Code Collaboration (NTCC) standards [12] and is available in the NTCC Model Library (w3.pppl.gov/NTCC). The MMM7.1 transport model has a single clearly defined interface, which facilitates porting the model to whole device modeling codes. In addition to its installation in the PTRANSP code, the MMM7.1 model has been ported to the Framework Application for Core-Edge Transport Simulations code (FACETS) [13], Automated System for TRansport Analysis code (ASTRA) [14], Tokamak Simulation Code (TSC) [15] and Simulation of Radio Frequency Wave Interactions with Magnetohydrodynamics code (SWIM) [16]. PTRANSP predictive simulations have been carried out using the MMM7.1 model for ITER target steady state and hybrid discharges [17–19]. An objective of this modeling is to prepare for the commissioning of ITER and to plan for the burn stages of ITER operation.

In this paper, electron and ion thermal transport in eight DIII-D, three JET and two TFTR L-mode tokamak discharges are investigated by comparing predictive PTRANSP simulation results for the evolution of electron and ion temperature profiles with experimental data. PTRANSP electron and ion temperature simulations are carried out using MMM7.1 anomalous transport model. Discharges with scans over gyroradius, ITER like current ramp-up, with and without neon impurity injection, collisionality, low and high plasma current are considered. The components of the MMM7.1 model provide contributions to transport in the different regions of plasma discharge. It is found in the simulations that the DRIBM contributes to the anomalous transport primarily near the edge of the plasma [20]. In that region the contributions from other sources of transport is negligible since transport associated with ITG and TE modes diminish as a function of radius and neoclassical ion thermal transport contributes mainly near the center of the discharge. Comparisons with data are made using simulations carried out with and without the DRIBM component within the MMM7.1 model. These comparisons illustrate the role played by the DRIBM component in the MMM7.1 model. The comparisons between simulations and data include the entire profiles from the magnetic axis to the plasma edge. Overall, good agreement with experimental data is found when the DRIBM model is included as a component of the MMM7.1 model [20].

The organization of the paper is as follows. In Section II, details are given regarding the experimental data for DIII-D, JET and TFTR L-mode discharges considered. In particular, the features of the thirteen different discharges, chosen for the study and validation of MMM7.1, are described. Section III contains a description of the protocol for running the PTRANSP predictive simulations. In Section IV, the transport coefficients, which are predicted by the MMM7.1 model and which are utilized in the simulations, are presented. Section V contains the simulation results, and the content of the paper is summarized in Section VI.

II. L-MODE EXPERIMENTAL DATA

The symbols used to denote various plasma variables, the units for these variables, and the variable definitions are presented in Table I. TRANSP (http://w3.pppl.gov/transp) processed and analyzed L-mode experimental data for eight DIII-D, three JET and two TFTR discharges are shown in Tables II and III. The features of the thirteen discharges are described in order to illustrate the variety of discharges chosen for examining the role of various components that are included in the MMM7.1 anomalous transport model.

DIII-D Discharges

Experimental data from eight DIII-D L-mode discharges spanning a variety of operating conditions are considered in this paper. Some of the relevant experimental parameters for the eight DIII-D L-mode discharges are listed in Table II.

Discharges 101381 and 101391 are part of a DIII-D ρ_* scan in which each discharge is designed to have the same plasma shape as well as the same plasma β, collisionality, safety factor aspect ratio and Mach number. As shown in the Table II the discharge 101381 and the discharge 101391 correspond to the high and low ρ_* scans respectively. Existing tokamaks can match all transport relevant local dimensionless parameters expected in reactor scale devices with the exception of ρ_*. Thus the scaling of transport with ρ_* is of central importance [21]. The ρ_* scan in 101381 and 101391 discharges was performed by varying the toroidal magnetic field and plasma current (to match magnetic-q) by a factor of 2, as has been the standard method in previous non-dimensional scaling experiments on DIII-

D [21, 22]. The resulting temperature and magnetic field variation changes ρ_* by a factor of roughly 1.6 in these scans.

The goal of ITER similar current ramp-up DIII-D L-mode experiments was to test whether the proposed ITER startup scenarios are feasible and to develop improvements in the ramp-up scenarios [23]. The discharges 132498, 136779, 132411, 136303 listed in Table II are ITER similar current ramp-up DIII-D L-mode discharges [23].

Discharge 98775 is a neon impurity injected discharge while in the discharge 98777 no neon impurity is injected. As it can be seen in Table II, the shape of the plasma (elongation and triangularity), toroidal magnetic field and plasma current are held nearly constant in these two discharges. However, the density and $Z_{\rm eff}$ are different, in discharges 98775 and 98777, due to the neon impurity injection. The purpose of these shots is to improve confinement mechanism with impurity injection, in particular, correlation with reduction of fluctuations and transport. The improvement is correlated with a reduction in ion and electron transport, with ion energy transport reduced to nearly neoclassical levels [24, 25]. Suppression of the long wavelength turbulence and transport reduction are attributed to the synergistic effects of impurity induced enhancement of $\mathbf{E} \times \mathbf{B}$ shearing rate and the reduction of toroidal drift wave turbulence growth rate.

A. JET and TFTR Discharges

Three JET L-mode discharges, 79575, 79811 and 79814, and two TFTR L-mode discharges, 45950 and 45980, are considered in this paper. Some of the relevant experimental parameters of these discharges are given in the Table III.

The JET discharge, 79575, is the stationary L-mode discharge where the beam configuration has been changed from tangential to normal in the middle of the current flat-top, leading to the strong reduction of the torque, beam driven current and toroidal rotation velocity.

The JET discharges 79811 and 79814 represent a collisionality scan carried out to study momentum transport [26]. Collisionality was varied by altering the electron temperature using neutral beam power at constant density while other dimensionless quantities, such as ρ_*, normalized plasma β_N, magnetic-q and ion to electron temperature ratio are kept as similar as possible [26, 27].

TFTR discharges 45950 and 45980 are high and low current L-mode discharges with balanced neutral beam heating shots [28, 29]. Data for these discharges are taken from the International Profile Database [30]. The density profiles in these two discharges are somewhat peaked, and the ratio of the central ion and electron temperatures (T_{i0}/T_{e0}) is approximately 5.4/6.8 keV. Inclusion of high and low current discharges in TFTR were carried out to illustrate the magnetic-q dependence of the transport model.

III. SIMULATION PROTOCOL

All the simulations are carried out using the time dependent PTRANSP integrated predictive modeling code (http://w3.pppl.gov.transp). TRANSP/PTRANSP is a time-dependent, 1 1/2-D tool for both interpretive and predictive simulations of tokamak discharges. In interpretive simulations, diffusion coefficients and fluxes are computed from the power balance equations given the computed power deposition profiles and the measured temperature profiles. Conversely, in predictive simulations, diffusion coefficients and fluxes are computed from theoretical models and used for a self-consistent solution of transport equations to compute the plasma profiles.

The PTRANSP code includes a wide variety of models for transport, sources, sinks, equilibrium, macroscopic instabilities and boundary conditions. Anomalous transport models in PTRANSP include Multi-Mode 7.1 (MMM7.1), the Gyro-Landau Fluid (GLF23), the Trapped Gyro-Landau Fluid (TGLF) [31], the older Multi-Mode model (MMM95), the gyro-Bohm model and the Coppi-Tang model. Options for neoclassical transport include the NEO, NCLASS, Chang-Hinton and Sauter models. Sources of heat, particles, momentum and current drive associated with neutral beam injection are described using the NUBEAM model. Many options are available for radio frequency heating and current drive and to compute the plasma equilibrium. Most models are available in the NTCC model library [12].

In this study, the PTRANSP code is used to compute the evolution of electron and ion temperature and magnetic-q profiles. Initial conditions and time dependent boundary conditions for the electron and ion temperatures are taken from experimental data, and the MMM7.1 anomalous transport model is utilized to compute electron and ion thermal transport. The neoclassical ion thermal transport, bootstrap current, and neoclassical electrical resistivity are all computed using the NCLASS model [32]. The TEQ model [33] is used to

compute the evolution of the equilibrium, and the NUBEAM Monte-Carlo model [34] is used to compute neutral beam injection heating and current drive. Electron density and toroidal frequency and effective plasma charge are taken from experimental data. Quasi-neutrality is employed to yield ion density. The Porcelli model [35] is used to trigger sawtooth crashes and the effect of each sawtooth crash is computed using the KDSAW model[36]. The evolution of the current density and magnetic-q profiles are computed by advancing the magnetic diffusion equation. The initial q-profile for JET discharges is obtained from an EFIT reconstruction, which is using magnetic probe measurements. The time evolution of predicted electron and ion temperatures profiles (obtained using the transport coefficients computed with the MMM7.1 transport model) are compared with corresponding DIII-D, JET and TFTR experimental profiles.

IV. TRANSPORT COEFFICIENTS

The MMM7.1 model is a combination of the Weiland ITG/TEM, the Rafiq DRIBM and the Horton ETG transport models. The effective diffusivities from these independently derived theory based transport models are added together. The development of MMM7.1 transport model results from using different sets of approximations to estimate the transport from distinct instabilities. These instabilities tend to dominate in various regions of the plasma. The extent of each region of dominance follows naturally from the characteristics of each model, rather than being imposed by arbitrary cut-offs or step functions.

The neoclassical transport coefficients and the anomalous MMM7.1 component diffusion coefficients are combined for the self-consistent solution of the transport equations yielding the plasma profiles obtained in the simulations described in Section V. The total electron thermal diffusivity is

$$\chi_{\rm e} = \chi_{\rm e}^{\rm WNC} + \chi_{\rm e}^{\rm W19} + \chi_{\rm e}^{\rm ETG} + \chi_{\rm e}^{\rm DRBM}, \tag{1}$$

and, similarly, the total ion thermal diffusivity is

$$\chi_{\rm i} = \chi_{\rm i}^{\rm WNC} + \chi_{\rm i}^{\rm W19} + \chi_{\rm i}^{\rm DRBM}. \tag{2}$$

The notation used in the diffusivity equations, Eqs. 1-2, is defined in Table IV.

V. SIMULATION RESULTS

PTRANSP integrated modeling simulations of electron and ion temperature profiles and magnetic-q profiles are carried out using the MMM7.1 anomalous transport model for DIII-D, JET and TFTR L-mode discharges listed in Tables II-III. These discharges represent scans in normalized gyroradius, ρ_* (DIII-D: 101381 and 101391); ITER similar current ramp-up (DIII-D: 132498, 136779, 132411 and 136303); neon impurity injection (DIII-D: 987775 and 98777); plasma current ramp-up (JET: 79575); collisionality, ν^* (JET: 79811 and 79814); and plasma current ramp-up and ramp-down (TFTR: 45950 and 45980).

The comparison of the simulated and experimental profiles for high ρ_* DIII-D discharge 101381 is shown in FIG. 1. Predictive simulations are carried out using the MMM7.1 transport model and using the MMM7.1 transport model with the DRIBM model excluded. Overall, reasonable agreement with experimental data is found when the MMM7.1 model is used. In Panel (c) of FIG. 1, it is seen that when the DRIBM model is not included as a component of the MMM7.1 transport model, there is shortfall in the contribution to ion transport in the edge region of the L-mode discharge resulting in an over-prediction of ion temperature.

The comparison of simulated and experimental ion and electron temperature as a function of radius and time for the low ρ_* DIII-D discharge 101391 and the components of electron thermal diffusivity as a function of radius at $t = 3.4$ sec are shown in Fig. 2. It can be seen in Fig. 2d that the diffusivity due to the ion temperature gradient and trapped electron modes ($\chi_{\rm e}^{\rm W19}$) diminish with increasing normalized radius, ρ, and that the $\chi_e^{\rm DRIBM}$ contribution is dominant at the outer 10% of the discharge. The ETG electron thermal diffusivity ($\chi_e^{\rm ETG}$) contribution to $\chi_{\rm e}$ is found to be larger than the Weiland contribution ($\chi_{\rm e}^{\rm W19}$) [37]. The neoclassical electron thermal diffusivity ($\chi_{\rm e}^{\rm WNC}$) is included in the simulations but not plotted in Fig. 2d since the neoclassical electron thermal transport is negligible and does not affect the simulated temperature profiles.

The comparison of the simulated and experimental ion temperatures and of the components of ion thermal diffusivity is presented in Fig. 3 for the current ramp-up discharge DIII-D 132498. In the Fig. 3b it is shown that the DRIBM ion thermal diffusivity increases towards the plasma edge and provides a non-zero contribution to the total thermal diffusivity in the outer 35% of the plasma. The ion thermal diffusivity from the Weiland model ($\chi_{\rm i}^{\rm W19}$

which is mainly a result of ITG/TEM modes) is marginally stable near the magnetic axis and increasingly deviates from marginal stability with increasing the normalized radius. The neoclassical ion thermal diffusivity ($\chi_{\rm i}^{\rm WNC}$) is found to be dominant in the deep core region of the plasma, where the contributions from other modes are negligible. In the Fig. 3c, it can be seen that the simulated and experimental ion temperature at $\rho = 0.75$ increase as a function of time. The increase in the ion temperature is due to the increase in plasma current with time.

For the ITER like plasma current ramp-up DIII-D discharge 132411, the comparison of simulated and experimental temperature profiles at $t = 0.56$ sec and at $t = 1.2$ sec and the contributions to ion and electron thermal diffusivities $t = 0.56$ sec are shown in Fig. 4. The discharge 132411 is the slower current ramp-up discharge in the ITER like current ramp-up series of three DIII-D discharges (132411, 136303 and 136779). All three discharges are simulated but only the results of the simulation of the 132411 discharge are presented since the results of other two discharges, 136303 and 136779, are found to be similar to the results for discharge 132411 presented here. In Panel (f) of Fig. 4 it is shown that at $t = 0.56$ sec, the contribution due to the ETG component of of electron thermal diffusivity ($\chi_e^{\rm ETG}$) is dominant. In general, the dominance of one mode of transport over another varies from one region of the plasma to another depending on plasma conditions. The total electron thermal diffusivity is found to be larger than the ion thermal diffusivity, which is consistent with the experimental measurements (not reported here) based on power balance analysis. In the power balance analysis, diffusion coefficients are computed from the power balance equations given the computed power deposition profiles and the measured temperature profiles.

The magnetic-q profile and the central ion and electron temperatures are shown in Panel (a) of Fig. 5 for the discharge 132411 discussed above. The evolution of the magnetic-q profiles is computed by advancing a magnetic diffusion equation. It is found that q-profile stays above unity during the discharge. Therefore, this discharge is not subject to the effects of sawteething. It has been found that the DRIBM transport increases with decreasing plasma current (q increases) [8]. Moreover, in the start of the plasma current ramp up phase, the DRIBM transport is found to contribute over a larger region of the plasma radius, but as the plasma current increases (q decreases) the region in which the DRIBM transport contributes decreases. The agreement between simulated and experimental central electron and ion temperatures as a function of time is illustrated in Panels (b) and (c) of

Fig. 5.

The profiles shown in Fig. 6 are for DIII-D discharge 98777, no neon impurity injected, and for DIII-D discharge 98775, neon injected. For the 98775, the neon is injected 2.0 Tℓ/s (torr liters per second) into the edge of the plasma at time t = 0.8 sec. These experiments were carried out to demonstrate improvement in confinement with impurity injection. It has been found in experiments and in our simulations that the neon injected DIII-D discharge shows reduction in transport. In the neon injected discharge both the simulated and experimental electron and ion temperature are found to be higher than in the corresponding discharge in which neon is not injected. The difference in simulated central and experimental ion temperatures depends somewhat on the choice of the diagnostic time.

Simulation results for the JET plasma current ramp-up discharge 79575, carried out using the anomalous transport model MMM7.1 are shown in Fig. 7. Comparison between simulation and experimental results is presented in Panels (a) and (b). Both the electron and ion thermal diffusivities are found to be increasing with increasing radius, Panel (c). Time evolution for the simulated and measured central electron and ion temperatures are presented in the Panels (e) and (f) of Fig. 7. The time evolution of the central temperatures indicate sawteething in this plasma current ramp-up discharge. The Porcelli model [35] is used to trigger sawtooth crashes with the times of the crashes taken from measurements, and the effects of each sawtooth crash are simulated using the KDSAW reconnection model of Kadomstev [36]. The flattening of central q-profile for the discharge 79575, shown in the Panel (d) of Figure 7, is a consequence of sawteething. The equilibrium reconstruction with EFIT constrained by the polarimetry and MSE measurements is not available for the discharge, so the simulated q-profile shown in the Panel (d) of Fig. 7, is not compared with the q-profile from EFIT.

Simulation and experimental profiles are shown in Fig. 8 for the JET low ν^* discharge 79811 and for the JET high ν^* discharge 79814. For the discharges 79811 and 79814, the measurements of ion temperature data near the plasma edge are not available so that, consequently, the electron edge temperature is used as the boundary condition for both the electrons and the ions in the simulations. Unlike the JET stationary L-mode, 79575, in the low and high ν^* discharges, 79811 and 79184, there is no indication of sawteething.

The simulated and experimental electron and ion temperatures are shown in Fig. 9 for TFTR plasma current ramp NBI heated L-mode high current discharge, 45950, and low

current discharge, 45980. These discharges are taken from the ITER Profile Database. The objective of these current ramp experiments carried out on TFTR was to examine the magnetic-q dependence of the transport model. The agreement of the simulated and experimental electron and ion temperatures is illustrated for the two TFTR discharges in Fig. 9. The simulated temperatures and corresponding experimental data are compared at time t = 4.2s when one discharge, 45950, is in the flattop phase (steady state) and the other discharge, 45980, is in the ramp down phase (transient phase). The q-profiles in these discharges are nearly the same in the core region, while they are different in the edge region. The differences in the q-profiles in the edge region, resulting from the decrease in current in the ramp down impacts the contribution to diffusivity provided by the DRIBM modes. Consequently, the DRIBM transport is found to be larger in the ramp down phase of the discharge. This result follows from the relationship between the value of q in the plasma edge region and the dependence of the DRIBM diffusivity on the plasma current. It is this relationship that impacts the agreement between the predicted and experimental profiles.

VI. SUMMARY AND DISCUSSION

The Lehigh fusion physics group has focused for a number of years on the development of a model for anomalous transport in tokamak plasmas. The focus has been on the use of the model (as well as on using models developed by others) in the predictive integrated modeling of tokamak discharges. The first model was released in 1995, MMM95, and was used until two to three years ago to the release of MMM7.1 model, which had a substantially improved physics basis. The MMM95 model was calibrated using experimental data, and coefficients for the transport associated with different modes were fixed in 1995. Once fixed in 1995, these coefficients remained unchanged in our studies until MMM7.1 was introduced. In MMM7.1 anomalous transport model, there are no parameters or coefficients introduced and associated with any of the theory based components of the model. All components of the Multi-Mode model are precisely those provided by the authors of the components used in the Multi-mode model. There are no adjustable parameters used to fit experiments. The goal is to continue to add to the physics basis of the transport model that describes anomalous particle, thermal and momentum transport, and when there are significant advances, to release new versions of the model.

A significant advancement associated with the MMM7.1 transport model is the inclusion of the DRIBM model which takes into account transport associated with drift resistive inertial ballooning modes without the use of any adjustable parameters. It is found in the simulations carried out using the MMM7.1 model that the transport due to drift resistive inertial ballooning modes dominate at the edge of the plasma where the collisionality and magnetic-q values are highest, while the ITG and TEM mode dominates in the plasma core. The ion thermal neoclassical transport is found to be dominant near the the magnetic axis.

Simulations of the evolution of a variety of L-mode discharges in DIII-D, JET and TFTR tokamak plasmas are carried out, and the evolution of temperature profiles obtained using the MMM7.1 anomalous transport model are compared with the corresponding experimental data. It is found that the inclusion of the DRIBM component in the MMM7.1 transport model improves the match between the simulation and experimental temperature profiles. The comparisons between simulations and data include the entire temperature profiles from the magnetic axis to the plasma edge and contribute to the validation of the MMM7.1 anomalous transport model.

ACKNOWLEDGEMENTS

This work was supported in part by the US Department of Energy under contract No. DE-FG02-92-ER54141 and was supported in part by EURATOM and carried out within the framework of the European Fusion Development Agreement. The views and opinions expressed herein do not necessarily react those of the European Commission.

---

[1] L. Luo, T. Rafiq, and A. Kritz, Computer Physics Communications **184**, 2267 (2013).

[2] G. Bateman, A. Kritz, J. Kinsey, A. Redd, and J. Weiland, Physics of Plasmas **5**, 1793 (1998).

[3] A. J. Redd, A. H. Kritz, G. Bateman, and J. E. Kinsey, Physics of Plasmas **4**, 2207 (1997).

[4] A. Pankin, G. Bateman, A. Kritz, M. Greenwald, J. Snipes, and T. Fredian, Physics of Plasmas **8**, 4403 (2001).

[5] I. Voitsekhovitch, G. Bateman, A. H. Kritz, and A. Pankin, Physics of Plasmas **9**, 4241 (2002).

[6] T. Onjun, G. Bateman, A. H. Kritz, and G. Hammett, Physics of Plasmas **9**, 5018 (2002).

[7] S. E. Snyder, A. H. Kritz, G. Bateman, T. Onjun, V. Parail, and EFDA JET Contributors, Physics of Plasmas **12**, 112508 (2005).

[8] T. Rafiq, G. Bateman, A. H. Kritz, and A. Y. Pankin, Physics of Plasmas **17**, 082511 (2010).

[9] J. Weiland, *Stability and Transport in Magnetic Confinement System*, Springer Series on Atomic, Optical and Plasma Physics Vol. 71 (Springer, 2012).

[10] W. Horton, P. Zhu, G. T. Hoang, T. Aniel, M. Ottaviani, and X. Garbet, Physics of Plasmas **7**, 1494 (2000).

[11] F. Jenko, W. Dorland, and G. Hammett, Phys. Plasmas **8**, 4096 (2001).

[12] A. Kritz, G. Bateman, J. Kinsey, A. Pankin, T. Onjun, A. Redd, D. McCune, C. Ludescher, A. Pletzer, R. Andre, L. Zakharov, L. Lodestro, L. Pearlstein, R. Jong, W. Houlberg, P. Strand, J. Wiley, P. Valanju, H. John, R. Waltz, J. Mandrekas, T. Mau, J. Carlsson, and B. Braams, Comput. Phys. Comm **164**, 108 (2004).

[13] J. R. Cary, J. Candy, R. H. Cohen, S. Krasheninnikov, D. C. McCune, D. J. Estep, J. Larson, A. D. Malony, A. Pankin, P. H. Worley, J. A. Carlsson, A. H. Hakim, P. Hamill, S. Kruger, M. Miah, S. Muzsala, A. Pletzer, S. Shasharina, D. Wade-Stein, N. Wang, S. Balay, L. McInnes, H. Zhang, T. Casper, L. Diachin, T. Epperly, T. D. Rognlien, M. R. Fahey, J. Cobb, A. Morris, S. Shende, G. W. Hammett, K. Indireshkumar, D. Stotler, and A. Y. Pigarov, Journal of Physics: Conference Series **125**, 012040 (2008).

[14] G. V. Pereverzev and P. N. Yushmanov, Preprint IPP Report 5/98 Garching (2002).

[15] S. Jardin, N. Pomphrey, and J. Delucia, Journal of Computational Physics **66**, 481 (1986).

[16] D. B. Batchelor, E. D'Azevedo, G. Bateman, D. E. Bernholdt, L. A. Berry, P. T. Bonoli, R. Bramley, J. Breslau, M. Chance, J. Chen, M. Choi, W. Elwasif, G.-Y. Fu, R. W. Harvey, W. A. Houlberg, E. F. Jaeger, S. C. Jardin, D. Keyes, S. Klasky, S. Kruger, L. P. Ku, D. McCune, J. Ramos, D. P. Schissel, D. Schnack, and J. C. Wright, Journal of Physics: Conference Series **78**, 012003 (2007).

[17] T. Rafiq, A. H. Kritz, C. Kessel, G. Bateman, D. C. McCune, and R. V. Budny, Phys. Plasmas **18**, 112508 (2011).

[18] A. H. Kritz, T. Rafiq, C. Kessel, G. Bateman, D. C. McCune, R. V. Budny, and A. Y. Pankin, Nuclear Fusion **51**, 123009 (2011).

[19] T. Rafiq, A. H. Kritz, C. E. Kessel, G. Bateman, D. C. McCune, R. V. Budny, and A. Y. Pankin, AIP Conf. Proc. **1392**, 92 (2012).

[20] T. Rafiq, A. Kritz, R. Budny, I. Voitsekhovitch, and A. Pankin, 24th IAEA Fusion Energy Conference San Diego, CA October 08-13 (2012).

[21] G. McKee, C. Petty, R. Waltz, C. Fenzi, R. Fonck, J. Kinsey, T. Luce, K. Burrell, D. Baker, E. Doyle, X. Garbet, R. Moyer, C. Rettig, T. Rhodes, D. Ross, G. Staebler, R. Sydora, and M. Wade, Nuclear Fusion **41**, 1235 (2001).

[22] C. C. Petty, T. C. Luce, K. H. Burrell, S. C. Chiu, J. S. deGrassie, C. B. Forest, P. Gohil, C. M. Greenfield, R. J. Groebner, R. W. Harvey, R. I. Pinsker, R. Prater, R. E. Waltz, R. A. James, and D. Wrblewski, Physics of Plasmas **2**, 2342 (1995).

[23] G. Jackson, T. Casper, T. Luce, D. Humphreys, J. Ferron, A. Hyatt, J. Leuer, T. Petrie, F. Turco, and W. West, Nuclear Fusion **49**, 115027 (2009).

[24] G. R. McKee, M. Murakami, J. A. Boedo, N. H. Brooks, K. H. Burrell, D. R. Ernst, R. J. Fonck, G. L. Jackson, M. Jakubowski, R. J. La Haye, A. M. Messiaen, J. Ongena, C. L. Rettig, B. W. Rice, C. Rost, G. M. Staebler, R. D. Sydora, D. M. Thomas, B. Unterberg, M. R. Wade, and W. P. West, Physics of Plasmas (1994-present) **7**, 1870 (2000).

[25] M. Murakami, G. McKee, G. Jackson, G. Staebler, D. Alexander, D. Baker, G. Bateman, L. Baylor, J. Boedo, N. Brooks, K. Burrell, J. Cary, R. Cohen, R. Colchin, J. DeBoo, E. Doyle, D. Ernst, T. Evans, C. Fenzi, C. Greenfield, D. Greenwood, R. Groebner, J. Hogan, W. Houlberg, A. Hyatt, R. Jayakumar, T. Jernigan, R. Jong, J. Kinsey, A. Kritz, R. L. Haye, L. Lao, C. Lasnier, M. Makowski, J. Mandrekas, A. Messiaen, R. Moyer, J. Ongena, A. Pankin, T. Petrie, C. Petty, C. Rettig, T. Rhodes, B. Rice, D. Ross, J. Rost, S. Shasharina, H. S. John, W. Stacey, P. Strand, R. Sydora, T. Taylor, D. Thomas, M. Wade, R. Waltz, W. West, K. Wong, L. Zeng, and D.-D. Team, Nuclear Fusion **41**, 317 (2001).

[26] T. Tala, A. Salmi, C. Angioni, F. Casson, G. Corrigan, J. Ferreira, C. Giroud, P. Mantica, V. Naulin, A. Peeters, W. Solomon, D. Strintzi, M. Tsalas, T. Versloot, P. de Vries, K.-D. Zastrow, and J.-E. contributors, Nuclear Fusion **51**, 123002 (2011).

[27] T. C. Luce, C. C. Petty, and J. G. Cordey, Plasma Physics and Controlled Fusion **50**, 043001 (2008).

[28] M. Zarnstorff and et al, IAEA Fusion Energy Conference **1**, 109 (1990).

[29] M. C. Zarnstorff, C. W. Barnes, P. C. Efthimion, G. W. Hammett, W. Horton, R. A. Hulse, D. K. Mansfield, E. S. Marmar, K. M. McGuire, G. Rewoldt, B. C. Stratton, E. J. Synakowski, W. M. Tang, J. L. Terry, X. Q. Xu, M. G. Bell, M. Bitter, R. V. Budny, C. E. Bush, P. H.

Diamond, R. J. Fonck, E. D. Fredrickson, H. P. Furth, R. J. Goldston, B. Grek, R. J. Hawryluk, K. W. Hill, H. Hsuan, D. W. Johnson, D. C. McCune, D. M. Meade, D. Mueller, D. K. Owens, H. K. Park, A. T. Ramsey, M. N. Rosenbluth, J. Schivell, G. L. Schmidt, S. D. Scott, G. Taylor, and R. M. Weiland, *in Proceedings of the 13th International Conference on Plasma Physics and Controlled Nuclear Fusion*, Wurzburg, 1990 (International Atomic Energy Agency, Vienna, 1991), Vol 1 pp 109-122.

[30] The ITER 1D Modelling Working Group:, D. Boucher, J. Connor, W. Houlberg, M. Turner, G. Bracco, A. Chudnovskiy, J. Cordey, M. Greenwald, G. Hoang, G. Hogeweij, S. Kaye, J. Kinsey, D. Mikkelsen, J. Ongena, D. Schissel, H. Shirai, J. Stober, P. Stubberfield, R. Waltz, and J. Weiland, Nuclear Fusion **40**, 1955 (2000).

[31] G. M. Staebler, J. E. Kinsey, and R. E. Waltz, Physics of Plasmas (1994-present) **14**, 055909 (2007).

[32] W. A. Houlberg, K. C. Shaing, S. P. Hirshman, and M. C. Zarnstorff, Physics of Plasmas (1994-present) **4**, 3230 (1997).

[33] L. L. LoDestro and L. D. Pearlstein, Physics of Plasmas (1994-present) **1**, 90 (1994).

[34] A. Pankin, D. McCune, R. Andre, G. Bateman, and A. Kritz, Computer Physics Communications **159**, 157 (2004).

[35] F. Porcelli, D. Boucher, and M. N. Rosenbluth, Plasma Physics and Controlled Fusion **38**, 2163 (1996).

[36] B. Kadomtsev, Sov. J. Plasma Phys. **1**, 389 (1975).

[37] T. Rafiq, A. Y. Pankin, G. Bateman, A. H. Kritz, and F. D. Halpern, Physics of Plasmas **16**, 032505 (2009).

Symbol	Unit	Definition
a	m	Plasma minor radius (half-width)
R	m	Major radius to geometric center of each flux surface
κ		Plasma elongation
δ		Flux surface triangularity at the edge
B_{T}	Tesla	Vacuum toroidal magnetic field at R
I_{p}	MA	Toroidal plasma current
$\bar{n}_{\mathrm{e},19}$	$10^{19}\mathrm{m}^{-3}$	Line averaged electron density
Z_{eff}		Effective charge of plasma
P_{NB}	MW	Injected neutral beam power at wall
T_{e}	keV	Electron temperature
T_{e0}	keV	Central electron temperature
T_{i}	keV	Ion temperature
T_{i0}	keV	Central ion temperature
ρ_{s}	m	Ion Gyroradius
ρ_*		Normalized gyroradius $[\rho_{\mathrm{s}}/a]$
β		Ratio of kinetic pressure to magnetic pressure
ν_*		Plasma collisionality

Table 1: Notation of plasma parameters used in this paper.

Tokamak	DIII-D	DIII-D	DIII-D	DIII-D	DIII-D	DIII-D	DIII-D	DIII-D
Discharge	101381	101391	132498	136779	132411	136303	98775	98777
Type	High ρ_*	Low ρ_*	ISCR	ISCR	ISCR	ISCR	Neon	No Neon
R (m)	1.65	1.65	1.70	1.75	1.74	1.74	1.66	1.67
a (m)	0.63	0.63	0.77	0.76	0.77	0.78	0.60	0.60
κ	1.54	1.54	1.78	1.75	1.80	1.75	1.68	1.68
δ	0.05	0.05	0.55	0.58	0.54	0.55	0.63	0.63
B_{T} (T)	1.03	2.07	2.14	1.90	2.16	1.90	1.57	1.58
I_{p} (MA)	0.65	1.30	1.64	1.45	1.10	1.40	1.19	1.18
$\bar{n}_{\mathrm{e},19}$	2.12	5.20	2.68	2.81	2.68	2.75	3.32	2.85
Z_{eff}	1.50	1.45	1.40	1.18	1.16	1.22	2.64	1.41
P_{NB} (MW)	1.85	6.10	0.19	1.40	1.80	1.30	4.89	5.03

Table 2: Plasma parameters for the DIII-D L-mode ρ∗, ITER similar current ramp-up (ISCR), neon injected impurity and no neon injected impurity scan discharges.

Tokamak	JET	JET	JET	TFTR	TFTR
Discharge	79575	79811	79814	45950	45980
Type	Stationary L-mode	Low ν^*	High ν^*	High I_p	Low I_p
R (m)	2.95	3.00	3.00	2.54	2.60
a (m)	0.98	0.98	0.98	0.80	0.80
κ	1.66	1.70	1.65	1.04	0.96
δ	0.23	0.26	0.23	0.00	0.00
B_T (T)	2.50	3.36	2.05	4.80	4.77
I_p (MA)	2.50	2.05	1.20	2.00	1.00
$\bar{n}_{\mathrm{e},19}$	2.00	1.60	1.55	3.30	3.42
Z_eff	2.00	1.55	1.35	2.72	2.46
P_NB (MW)	3.00	6.25	3.00	11.4	11.4

Table 3: Plasma parameters for the JET and TFTR L-mode discharges with I_p ramp-up, low ν^*, high ν^*, high I_p and Low I_p.

Symbol	Unibt	Definition
χ_e	m^2/s	Total electron thermal diffusivity
$\chi_\mathrm{e}^\mathrm{WNC}$	m^2/s	Neoclassical electron thermal diffusivity
$\chi_\mathrm{e}^\mathrm{W19}$	m^2/s	Electron thermal diffusivity from the Weiland model
$\chi_\mathrm{e}^\mathrm{ETG}$	m^2/s	Electron thermal diffusivity from the Horton ETG model
$\chi_\mathrm{e}^\mathrm{DRBM}$	m^2/s	Electron thermal diffusivity from the DRIBM model
χ_i	m^2/s	Total ion thermal diffusivity
$\chi_\mathrm{i}^\mathrm{WNC}$	m^2/s	Neoclassical ion thermal diffusivity
$\chi_\mathrm{i}^\mathrm{W19}$	m^2/s	Ion thermal diffusivity from the Weiland model
$\chi_\mathrm{i}^\mathrm{DRBM}$	m^2/s	Ion thermal diffusivity from the DRIBM model

Table 4: Symbols, units and definitions for the total electron and ion thermal diffusivities, neoclassical ion thermal diffusivity, and diffusivities associated with components of the MMM7.1 model.

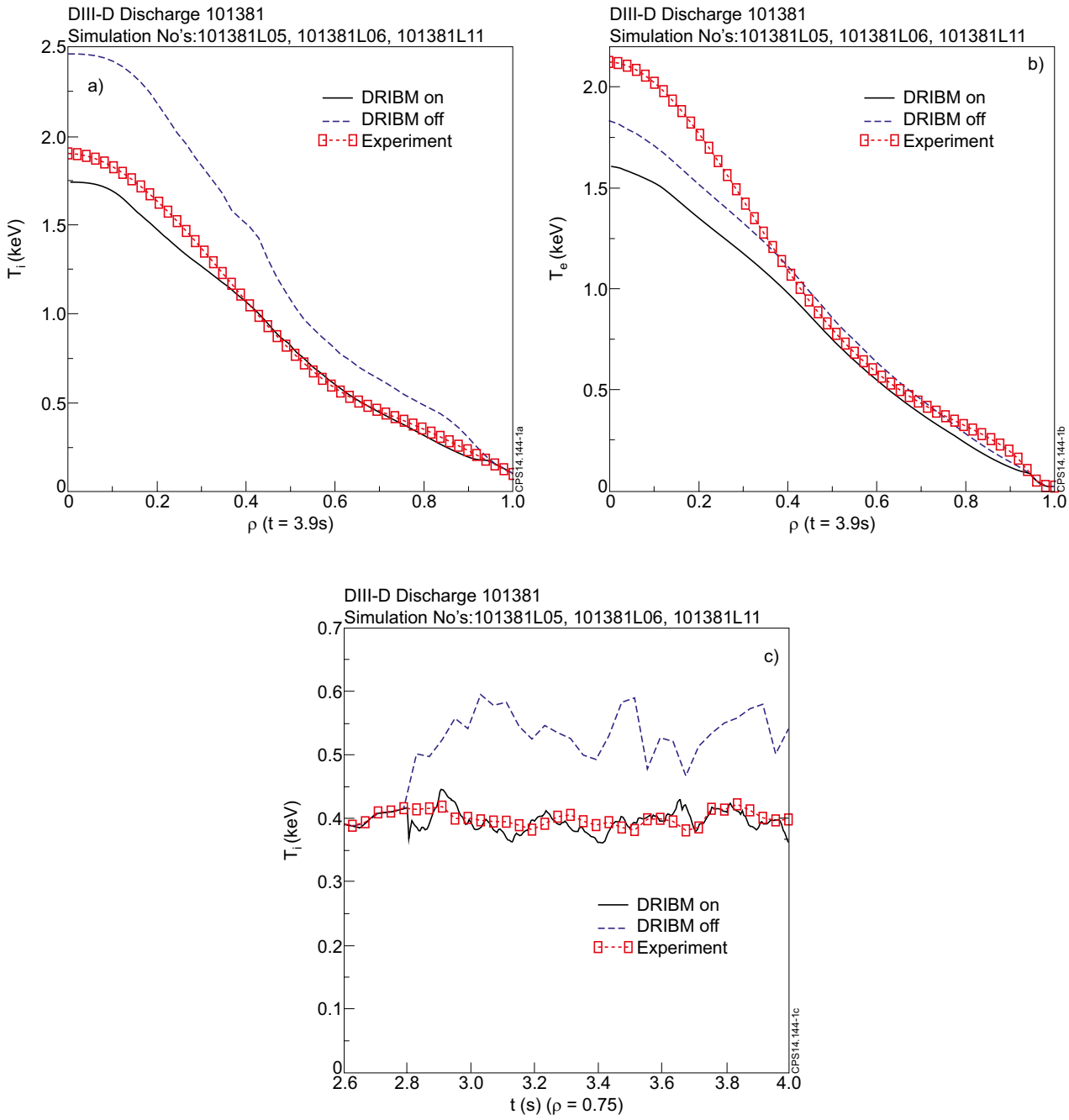

Figure 1: (Color online) Simulation results for the DIII-D high ρ∗ discharge, 101381. The ion temperature, in Panel (a), and the electron temperature, in Panel (b), are shown as a function of normalized minor radius (ρ) at time t = 3.9sec. In Panel (c) the ion temperature, at the normalized radius ρ = 0.75, is shown as a function of time. In each panel, results obtained using the MMM7.1 model is indicated by a solid line; results obtained when the DRIBM model is excluded from the MMM7.1 model is indicated by a dashed line; and the experimental results are indicated by a square-dashed line.

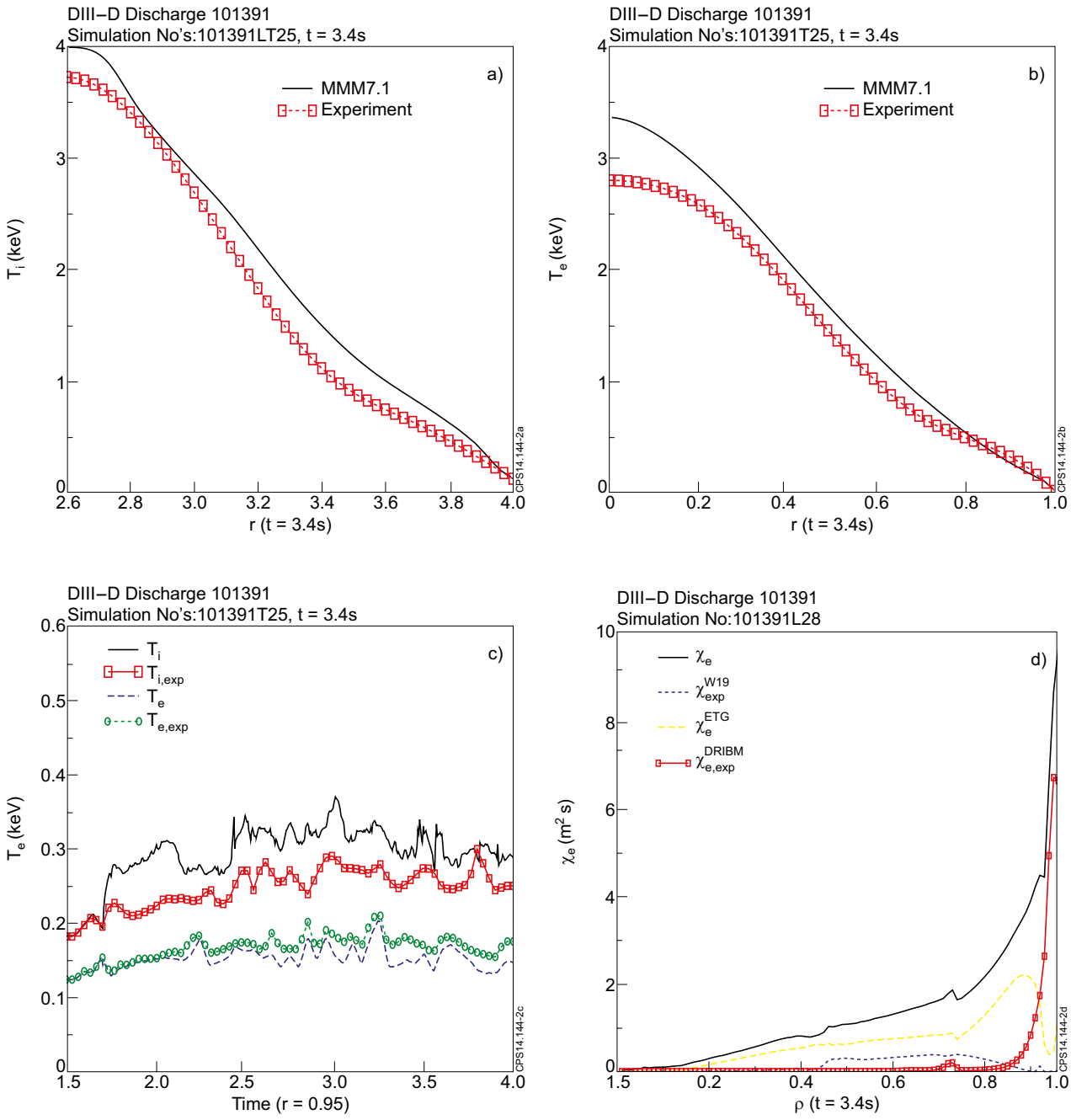

Figure 2: (Color online) Simulation results for the DIII-D low ρ∗ discharge, 101391. The predicted (solid line) and experimental (square-dashed line) ion and electron temperatures are shown in Panels (a) and (b), respectively, as a function of normalized minor radius (ρ) at time t = 3.4sec. In Panel (c) the ion and electron temperatures, at the normalized radius ρ = 0.95, are shown as a function of time. In Panel (d) the MMM7.1 component contributions to electron thermal transport are plotted as a function of radius at t = 3.4sec.

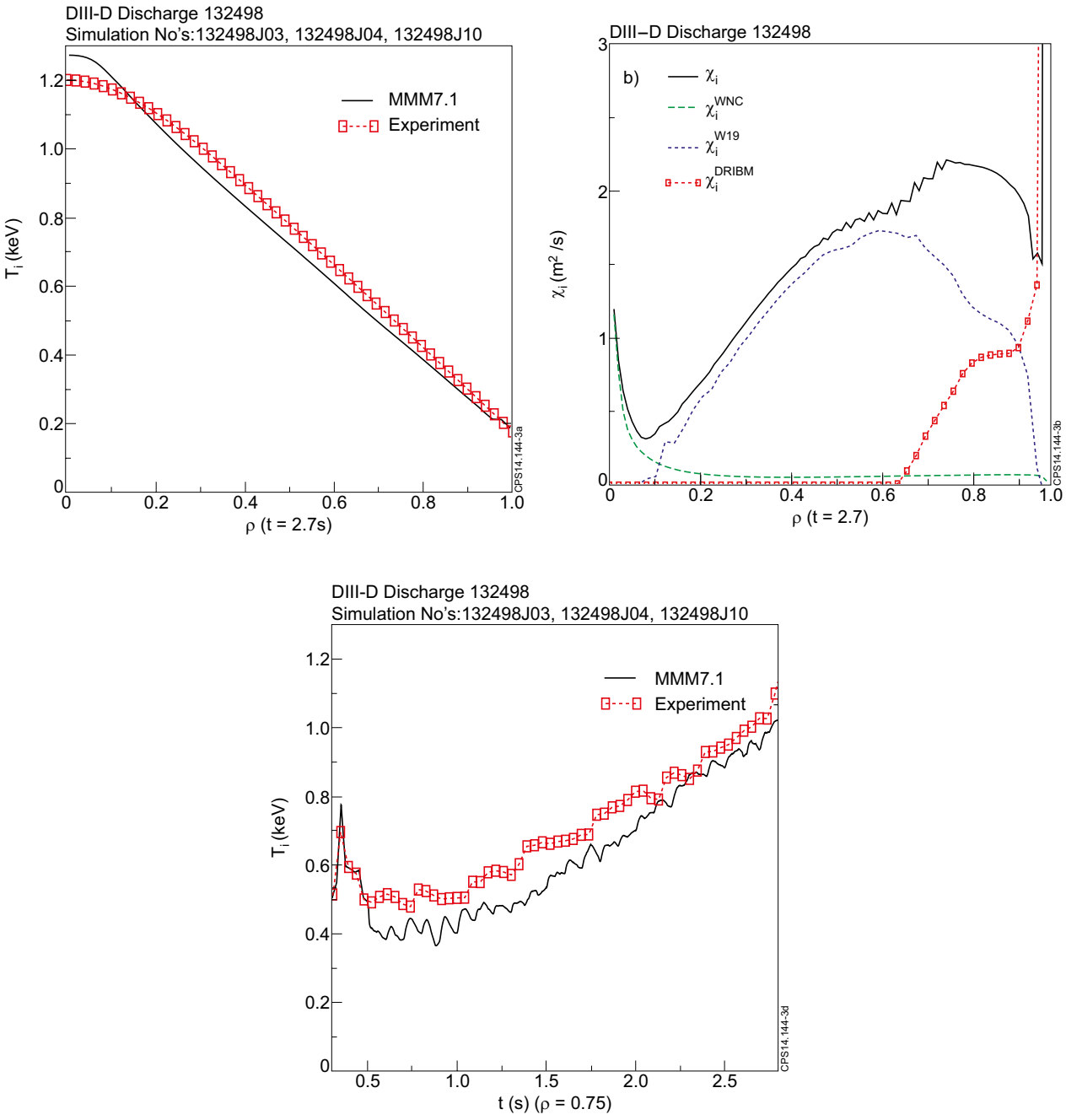

Figure 3: (Color online) ITER similar current ramp-up DIII-D discharge 132498. The predicted (solid line) and experimental (square-dashed line) ion temperature, Panel (a), and the MMM7.1 component contributions to ion thermal transport, Panel (b), are plotted as a function of radius at t = 2.7sec. In Panel (c) the predicted and experimental ion temperatures, at the normalized radius ρ = 0.75, are shown as a function of time.

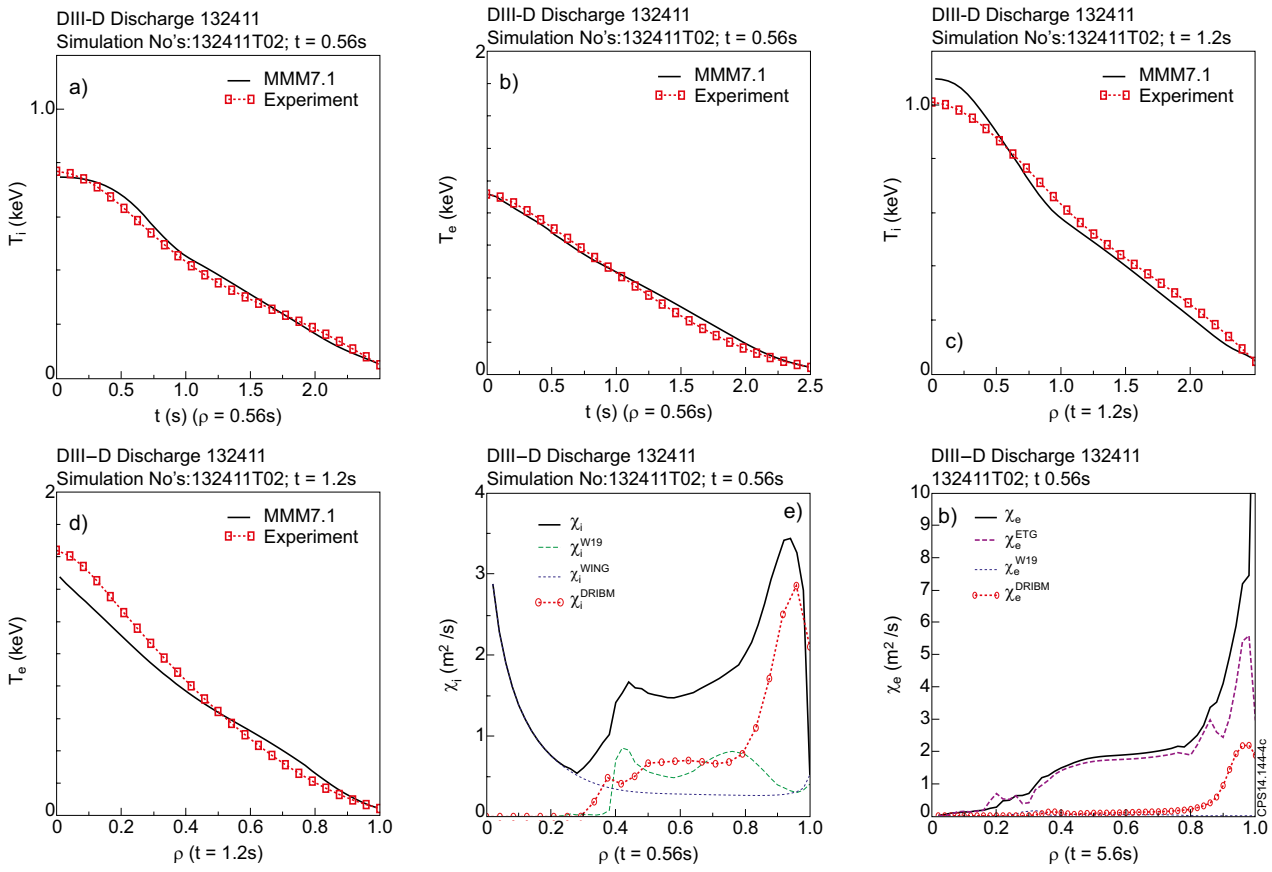

Figure 4: (Color online) ITER similar current ramp-up discharge DIII-D 132411. The predicted (solid line) and experimental (suare-dashed line) ion temperature, Panel (a), and electron temperature, Panel (b) are plotted as a function of radius at t = 0.56sec. Similar results are shown in Panels (c) and (d) at t = 1.2sec. The MMM7.1 component contributions to ion thermal transport, Panel (e), and to electron thermal transport, Panel (f) are plotted as a function of normalized radius at t = 0.56sec.

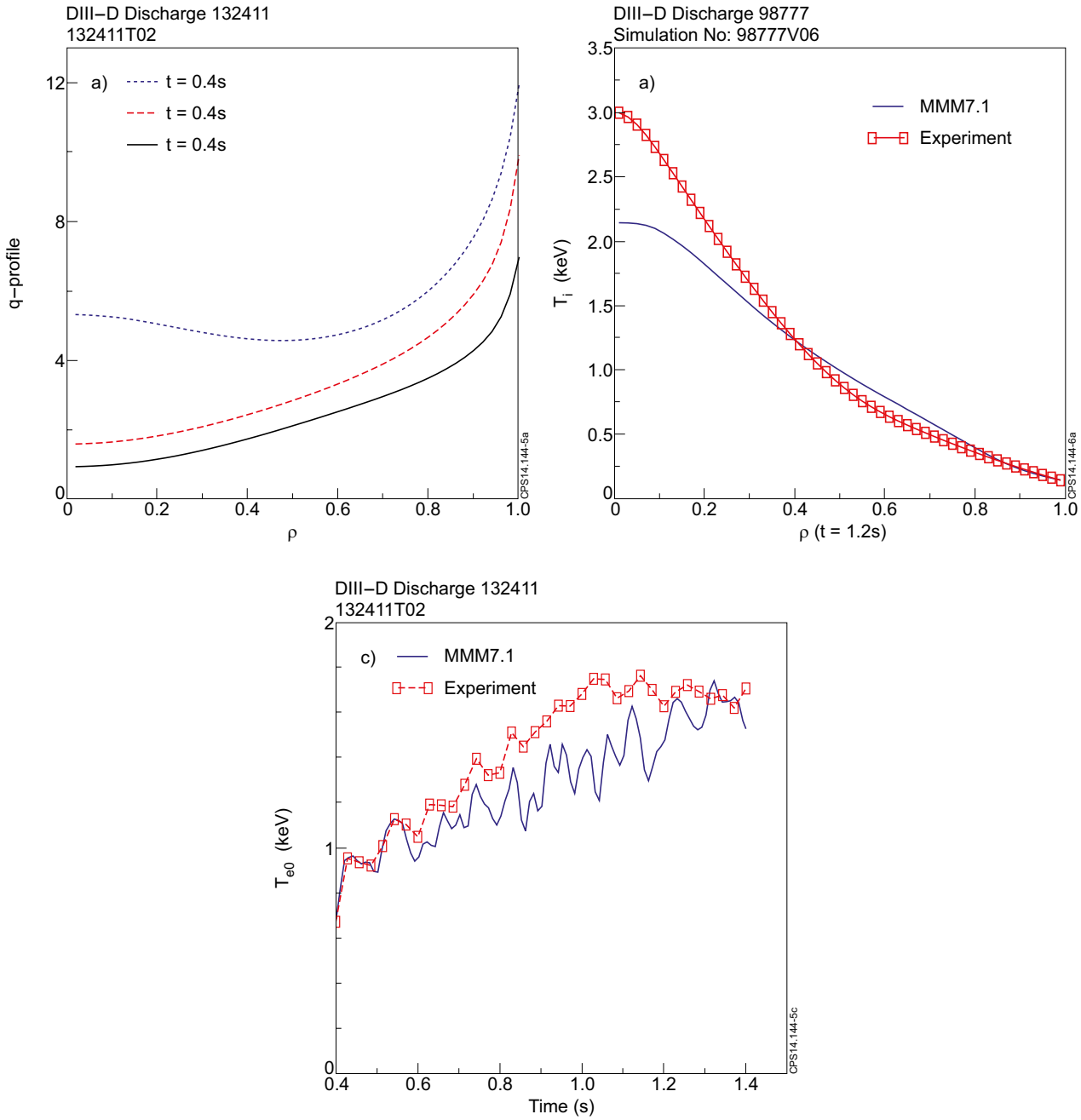

Figure 5: (Color online) The magnetic-q profile for the ITER similar current ramp-up discharge DIII-D 132498 is shown in Panel (a) as a function of normalized minor radius (ρ) at times t = 0.4sec, t = 0.8sec and t = 1.2sec. In Panel (b), the central ion temperature and, in Panel (c), the central electron temperature is plotted versus time. In the Panels (b) and (c), the square dashed curve represent experimental data the solid curves are the results of simulations using the MMM7.1 anomalous transport model.

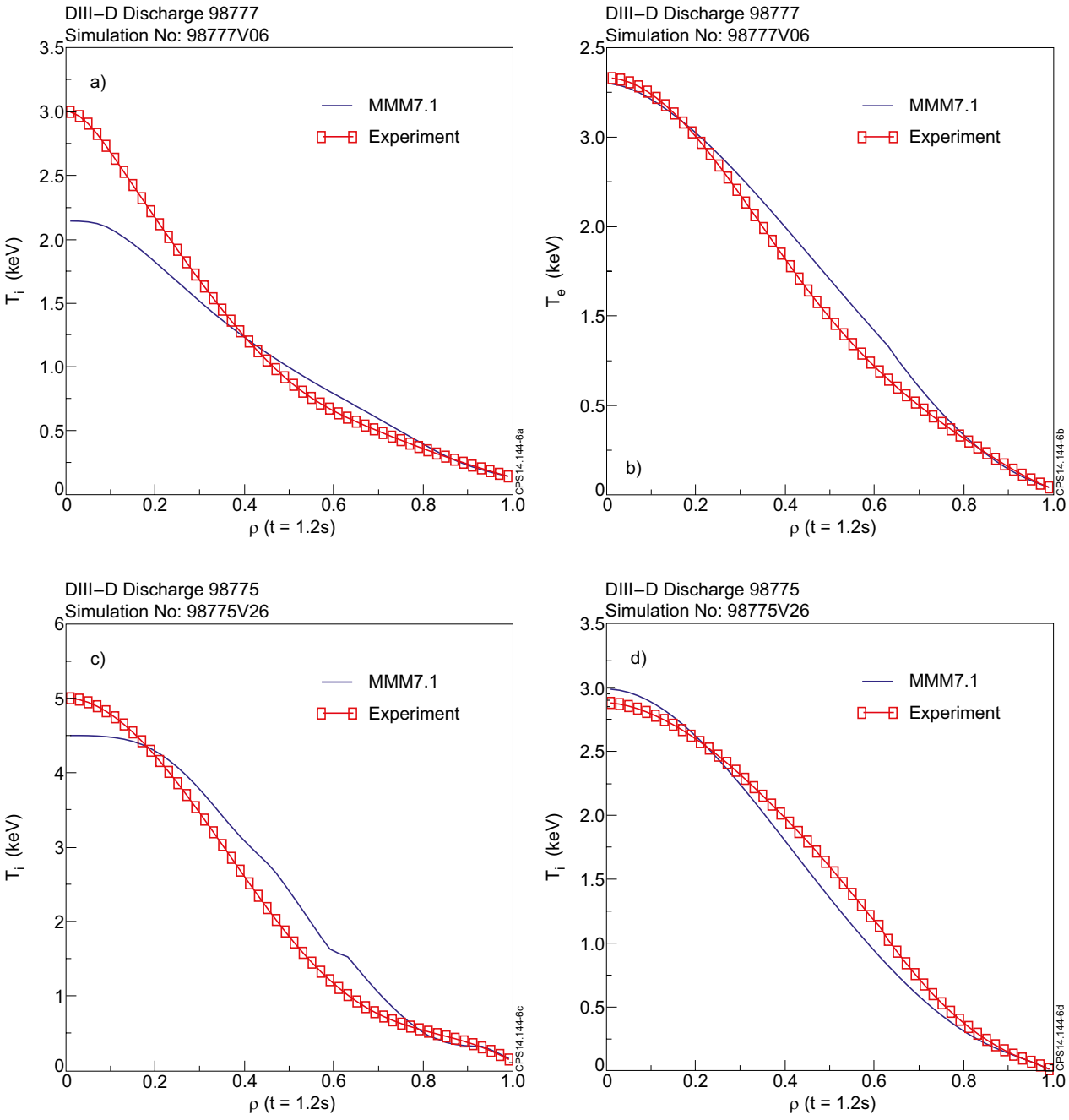

Figure 6: (Color online) The ion and electron temperatures, in Panels (a) and (b) for the no neon injected DIII-D discharge 98777 and in Panels (c) and (d) for the neon injected DIII-D discharge 987775 are plotted as a function of normalized minor radius (ρ) at time t = 1.2sec.

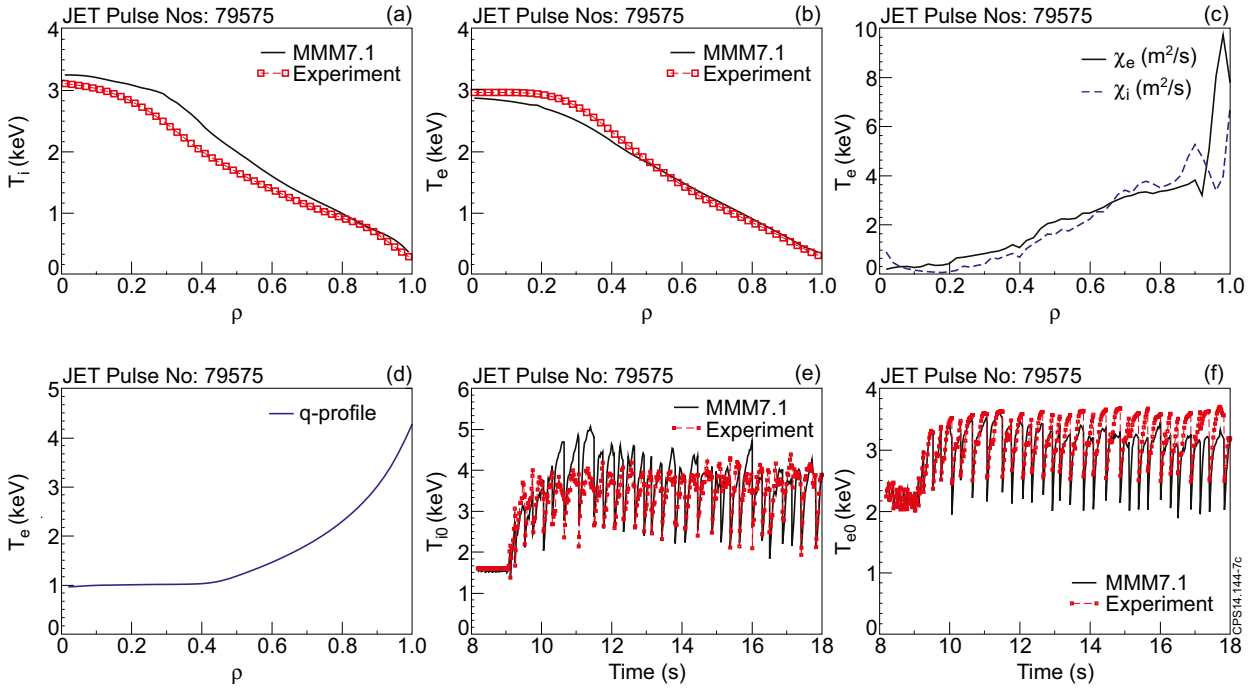

Figure 7: (Color online) For the JET plasma current ramp-up L-mode discharge, 79575, the ion temperature, Panel (a), the electron temperature, Panel (b), the total ion and electron thermal diffusivity, Panel (c), and the magnetic-q, Panel (d), are plotted as a function of normalized minor radius (ρ) at time t = 13sec. The central ion and electron temperatures are shown in Panels (e) and (f) as function of time. The square dashed curves represent experimental data and the solid curves are the results of simulations using the MMM7.1 anomalous transport model.

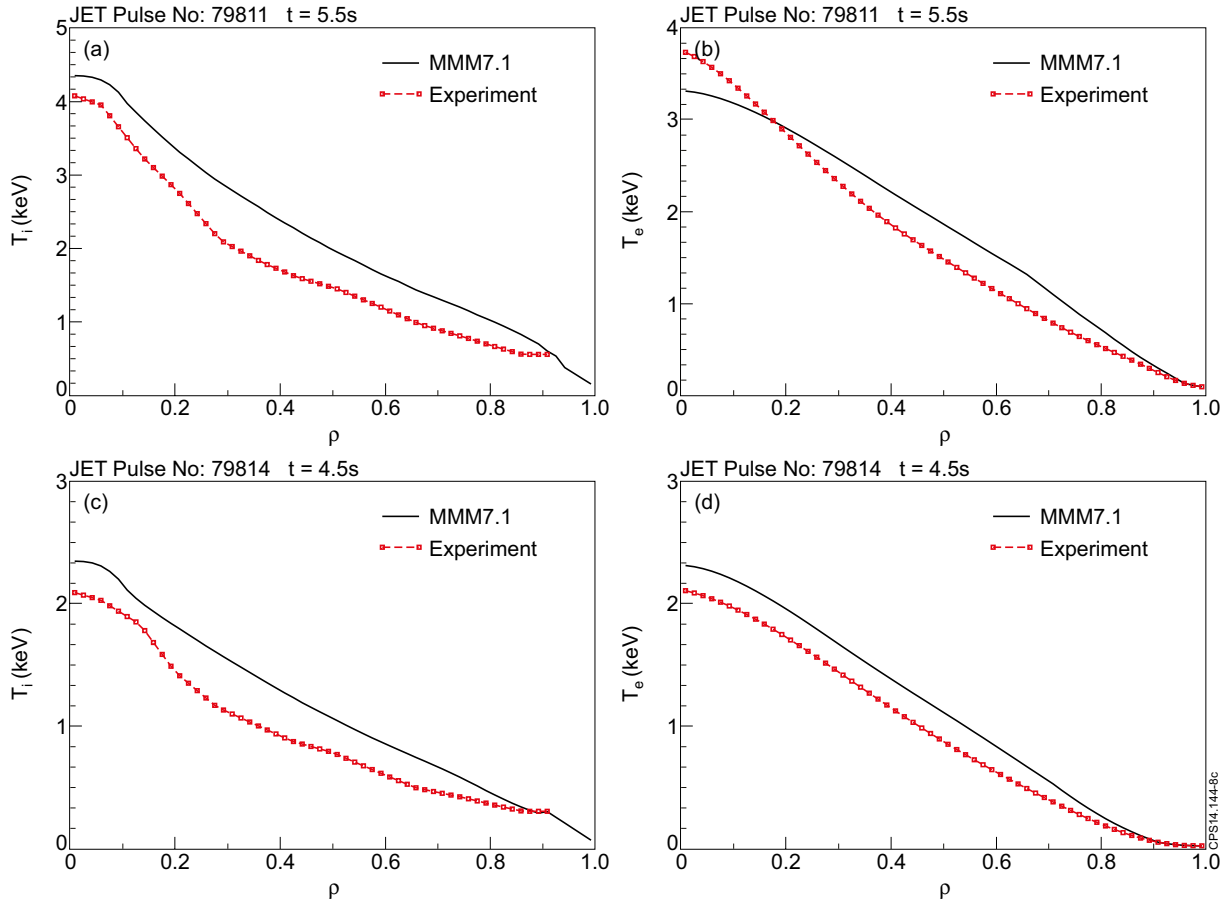

Figure 8: (Color online) The simulated and experimental ion and electron temperatures for the low ν^* JET discharge, 79811, are shown in Panels (a) and (b) as a function of normalized minor radius (ρ) at time t = 5.5sec. The simulated and experimental ion and electron temperatures for the high ν^* JET discharge, 79814, are shown in Panels (c) and (d) as a function of normalized minor radius (ρ) at time t = 4.5sec. Since for these discharges, measurements of ion temperature are not available near the plasma edge, the electron edge temperature is used as the boundary condition for both the electrons and the ions in the simulations.

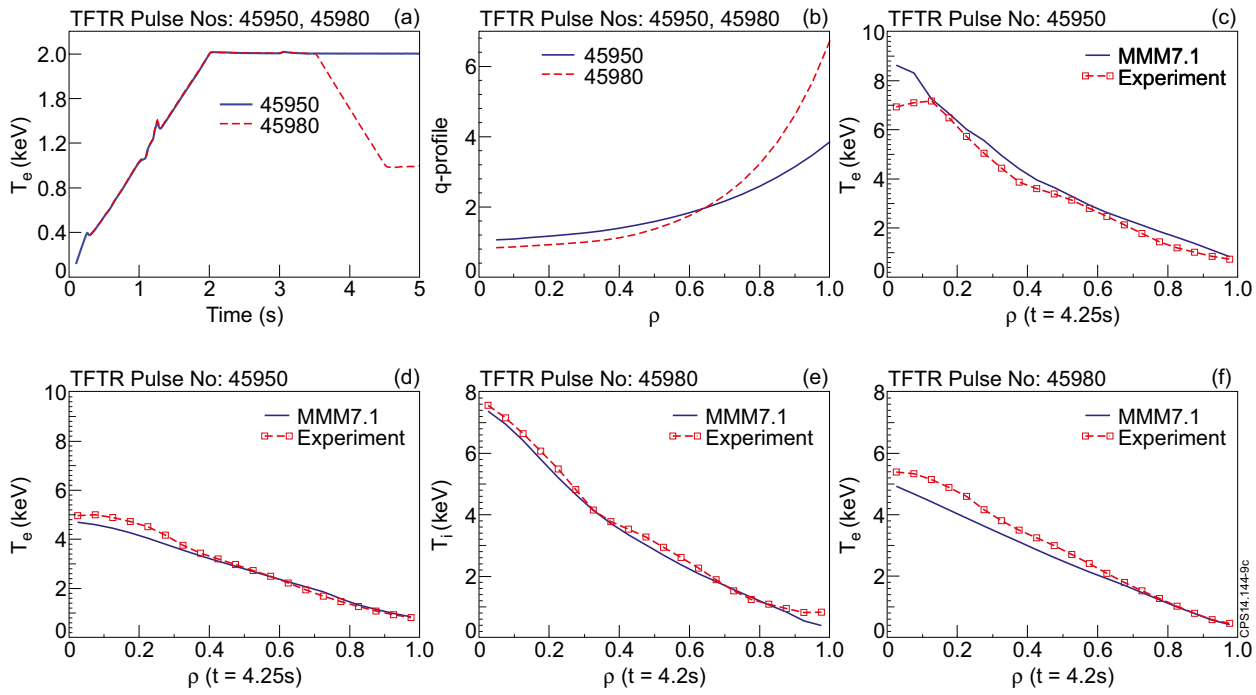

Figure 9: (Color online) (a) The plasma current as a function of time (b) magnetic-q profiles as a function of normalized minor radius (ρ) at time t = 4.2s for the two TFTR discharges 45950 and 45980. (c) Ion temperature (d) electron temperature as a function of normalized minor radius (ρ) at time t = 4.25s for simulation of the high I_p discharge TFTR 45950. (e) Ion temperature (f) electron temperature as a function of normalized minor radius (ρ) at time t = 4.2s for simulation of the low I_p discharge TFTR 45980.